Article

Geometric and Electronic Structure of #-Oxygen Sites in Mn-ZSM-5 Zeolites

Daniel Radu, Pieter Glatzel, Alexandre Gloter, Odile Stephan, Bert M. Weckhuysen, and Frank M. F. de Groot

J. Phys. Chem. C, **2008**, 112 (32), 12409-12416 • DOI: 10.1021/jp802915k • Publication Date (Web): 23 July 2008

Geometric and Electronic Structure of α-Oxygen Sites in Mn-ZSM-5 Zeolites

Daniel Radu,[†] Pieter Glatzel,[‡] Alexandre Gloter,[§] Odile Stephan,[§] Bert M. Weckhuysen,[†] and Frank M. F. de Groot*,[†]

Inorganic Chemistry and Catalysis Group, Department of Chemistry, Utrecht University, Sorbonnelaan 16, 3584 CA Utrecht, The Netherlands, European Synchrotron Radiation Facility (ESRF), BP 220, 38043 Grenoble Cedex 9, France, and Laboratoire de Physique des Solides, Université Paris-Sud, 91405 Orsay, France

Received: April 4, 2008; Revised Manuscript Received: May 23, 2008

It is shown that α-oxygen sites are generated by the decomposition of N_2O in ion-exchanged Mn-ZSM-5 zeolites. The catalytic activity decreases to zero in 1 h, and the amount of α-oxygen that is formed is reduced from ∼30% α-oxygen sites per Mn atom in the initial N_2O treatment to a value of ∼4% in the subsequent cycles. The catalytic activity correlates with the intensity of a UV−vis band located at 18 500 cm^{-1}, suggesting that the α-oxygen sites are linked to Mn sites with a distorted tetragonal symmetry with extended Mn−O bonds with respect to bulk oxides. Scanning transmission electron microscopy with electron energy loss spectroscopy (STEM−EELS) results indicate that the Mn sites are distributed unevenly over the ZSM-5 crystals, where most Mn atoms are found in the top ∼2 nm from the crystal surface. The X-ray absorption spectroscopy (XAS) spectra indicate that, under reaction conditions, the Mn atoms have a 5-fold coordination and a valence of ∼2.5, which is little affected by the N_2O and NO treatments as only ∼4% of these sites is active.

1. Introduction

In 1993, Panov et al.[1] published a paper in which Fe-ZSM-5 materials were used to oxidize benzene to phenol in one step at room temperature. They showed that Fe-ZSM-5 can generate an α-oxygen form similar to its biological analog methane mono-oxygenase (MMO), where Fe-ZSM-5 uses N_2O instead of O_2 as the source of oxygen. This discovery led to a large number of studies to identify the active phase and the nature of α-oxygen in Fe-ZSM-5 and related systems.[2–10] Panov defines α-oxygen as isolated ions or small complexes inside the ZSM-5 channels. The active site is often visualized as a binuclear iron center, based on extended X-ray absorption fine structure (EXAFS) analysis and also on the occurrence of such sites in MMO. The evidence is as yet not convincing as has been discussed by Heijboer et al.[11,12] Studies show that α-oxygen is able to yield single oxygenated compounds from alkanes[13] and halogen−aromatic compounds.[14] In addition, Fe-ZSM-5 has been used to create C−H bonds, for example, for methane-to-benzene conversion.[15] The selective oxidation studies also revealed that Fe-ZSM-5 is active in the N_2O decomposition reaction.[16–20] Finally, this activity toward nitrogen-containing compounds makes Fe-ZSM-5 an eligible candidate for the removal of nitrogen oxides by selective catalytic reduction (SCR).[21–25]

The general reaction scheme of the active site in Fe-ZSM-5 can be represented by two connected reactions:

$$N_2O + \underline{\alpha} \rightarrow \alpha\text{-}O + N_2 \quad \text{(I)}$$

$$C_xH_y + \alpha\text{-}O \rightarrow \underline{\alpha} + \text{“}C_xH_yO\text{”} \quad \text{(II)}$$

In reaction I, a nitrous oxide, usually N_2O is stripped of its oxygen at a α-vacancy (α) thereby creating an α-oxygen site (α-O). In reaction II, the α-oxygen site subsequently oxidizes a hydrocarbon to a, selectively, oxidized hydrocarbon. In methane oxidation, reaction I provides the α-oxygen sites needed for the selective oxidation, and in SCR de-NOx the α-vacancies are created by reducing the α-oxygen sites by hydrocarbons.

In addition to Fe-ZSM-5, also Cu-ZSM-5 materials can generate α-oxygen. For example, Chajar et al.[26] present the oxidation of C_3H_8 on Cu-ZSM-5 using NO or O_2 as an oxygen source. Cu-ZSM-5 is used to oxidize organic substrates, including phenol[27] and methane.[28] Studies using different characterization techniques identified the active center to be a bis(μ-oxo) complex similar to that present in enzyme systems. For example, Groothaert and co-workers[29–31] found a clear correlation between the UV−vis band and the oxidation state of copper in Cu-ZSM-5 zeolites. They assigned the observed 22 700 cm^{-1} UV−vis band from Cu-ZSM-5 to a bis(μ-oxo) dicopper core formed using the oxygen released during the N_2O decomposition. The oxidation state of the Cu was found to change from Cu^I to Cu^{II} with the introduction of N_2O and back to Cu^I after removal of the oxygen. The oxygen released during the N_2O decomposition has a special nature due to the high reactivity character and is known as α-oxygen species. The reactivity of Cu-ZSM-5 was used to selectively oxidize methane to methanol in a one-step reaction.[28]

Manganese oxides are known for their oxidation−reduction chemistry, based on which Yamashita and Vannice[32] showed that they are active in N_2O decomposition. It was also shown that N_2O decomposition occurs over all Mn oxides, but stable behavior was observed only for Mn_2O_3 and Mn_3O_4. The reactivity of these manganese oxides can be extended to the SCR methods of NO_x removal with ammonia.[33–39] Experiments by Cimino et al.[40] and Stone[41] show that by introducing low amounts of transition metal ions in inert oxide matrixes (<1 transition metal ion per 100 cations), the catalytic activity increases. At higher transition metal ion amounts, the activity resembles that of the corresponding pure oxides.

* Corresponding author. E-mail: f.m.f.degroot@uu.nl.
† Utrecht University.
‡ European Synchrotron Radiation Facility.
§ Université Paris-Sud.

10.1021/jp802915k CCC: $40.75
Published on Web 07/23/2008

In this paper, we first show the catalytic data showing that α-oxygen sites exist in Mn-ZSM-5 zeolites after N_2O decomposition. Next, we characterize these active sites and show that the UV−vis spectra contain a dominant band that correlates with catalytic activity. The materials are further studied with a scanning transmission electron microscope (STEM) equipped with electron energy loss spectroscopy (EELS) and with high-resolution X-ray absorption at the Mn K edge.

2. Experimental Section

2.1. Catalyst Preparation. A series of Mn-ZSM-5 zeolites differing in their Mn/Al molar ratios have been prepared via ion exchange starting from NH_4-ZSM-5 (ZEOLIST, Si/Al ratio of 17.5, surface area of 361 m^2/g, and pore volume of 0.124 cm^3/g). As a manganese source, manganese acetate tetrahydrate ($Mn(ac)_2 \cdot 4H_2O$) (99+%, Acros) was used. The ion-exchange step was carried out for 24 h at a pH of 6.5 in a stirring reactor placed in a double-wall vessel connected to a water bath to maintain a constant temperature of 343 K. After ion exchange, the zeolite samples were washed with deionized water and dried at 373 K for 24 h. Before calcination the samples were pressed and sieved to obtain a particle size fraction between 150 and 212 μm. For sample activation, a procedure denoted as "mild calcination" was applied and consists of heating up the sample to 823 K with a ramp of 0.5 K/min in an 800 mL/min flow of N_2. At 473 K, 200 mL/min O_2 flow has been introduced to the gas mixture. Once a temperature of 823 K was reached the zeolite sample was kept under the same experimental conditions for 3 h, after which the zeolite sample was cooled down to room temperature with a ramp of 10 K/min. After each step in the catalyst preparation procedure, the samples were measured with X-ray diffraction (XRD). As reference compounds for these XRD measurements the following oxides were selected: MnO (99%, Aldrich), Mn_2O_3 (99%, Aldrich), and MnO_2 (99.99%, Aldrich). The N_2O and NO gases have been used as 10% diluted in helium (Linde). N_2O and NO had a purity of 2.0, and the He a purity of 4.5. The gases have been further diluted with pure He as indicated below.

2.2. Catalyst Testing. Catalytic activity of the zeolite sample with a particle size between 150 and 212 μm was measured using a quartz flow reactor in which typically 0.1 g of catalyst was placed on a frit. The reactor was placed in an oven that can be controlled within ±1 K from the desired temperature using a West 6810 temperature controller. Concentrations and flow rate (total flow rate of 80 mL/min) were controlled with Brooks mass flow controllers. The inlet concentration of N_2O was 3750 ppm balanced with He until the desired flow. When NO was used, the inlet concentration of NO was 3750 ppm balanced with He. Before each run the catalyst was pretreated by heating up to 673 K in He flow and kept there for 1 h. Then the catalyst was cooled down to the reaction temperature. A typical catalytic experiment consists of exposures to N_2O for 1 h, followed for 10 min of flushing with He to eliminate the traces of N_2O from the system. At the end of the flushing period, 3750 ppm of NO was introduced in the gas flow for 1 h, followed again by a 10 min period of flushing with He. These steps were repeated three times, giving three consecutive cycles of N_2O/NO treatments. Product analysis was carried out using an Interscience Compact GC system, equipped with two different columns (a Molsieve 5A and a Porabond Q) each having a thermal conductivity (TCD) detector. In addition, a Thermo Environment Instruments 42C NO_x chemiluminescence analyzer was connected in parallel with the GC to determine the NO and NO_x concentrations and could be operated simultaneously.

2.3. Catalyst Characterization. ***2.3.1. X-Ray Diffraction.*** XRD patterns of the zeolite samples were measured using an Enraf-Nonius CPS 120 powder diffraction apparatus with Co Kα radiation ($\lambda = 1.789$ Å). The XRD results gave for all cases an equivalent ZSM-5 pattern within the accuracy of the equipment. This indicates that all samples have the MFI structure with identical cell dimensions.

2.3.2. X-Ray Fluorescence (XRF). Elemental analysis was carried out using a Goffin Meyvis spectroX-laboratory 2000 XRF spectrometer. The XRF results indicated that the Si/Al ratio was unchanged from the starting material value of 17.5 for all samples. The Mn/Al ratio was, respectively, 0.13, 0.15, 0.19, 0.22, 0.24, 0.26, and 0.30. Because the Si/Al ratio is 17.5, as also confirmed from XRF, the Mn weight loading is approximately 5 times the value Mn/Al ratio, i.e., a Mn/Al ratio of 0.24 yields a Mn concentration of 1.20 wt %, etc. We have used these Mn/Al ratios to set the sample codes to MnZ-0.13, etc.; the sample without manganese is indicated as MnZ-0.00.

2.3.3. Diffuse Reflectance Spectroscopy (DRS). After activation the zeolite samples were introduced in a quartz flow cell equipped with a UV−vis transparent window. Two O-ring valves were used to make the cell airtight and allow us to make in situ measurements. All Mn-containing samples after dehydration were treated for 1 h in an 80 mL/min flow of 0.375% N_2O/He at 623 K. The cell was closed, and a UV−vis spectrum was recorded. After this, the cell was flushed with He for 10 min to remove the traces of N_2O and an 80 mL/min flow of 0.375% NO/He was introduced for another hour. This procedure was repeated three times, and after each treatment DRS spectra of the catalyst sample were measured. UV−vis DRS spectra were recorded on a Varian Cary 500 spectrometer in the range of 5000−50 000 cm^{-1} (200−2200 nm). In order to eliminate the potential spectral contributions of the zeolite material, a spectrum of the quartz cell containing a dehydrated ZSM-5 zeolite sample was used as a white reference standard.

2.3.4. Scanning Transmission Electron Microscope with Electron Energy Loss Spectroscopy. STEM−EELS measurements were performed in Orsay (France) with a 100 keV STEM instrument (VG HB 501) equipped with a field emission electron source. Mounted on the STEM instrument was a parallel electron energy loss spectrometer (Gatan 666) optically coupled to a charge-coupled device (CCD) camera generating an EELS spectrum with a 0.5−0.7 eV energy resolution and 0.5 nm spatial resolution within a typical acquisition time down to 1 ms per pixel.[21,42] In these experiments, the oxygen K edge, silicon L edge, and manganese L edge were monitored. The solids were first sonicated in ethanol and then dropped on a holey amorphous carbon film supported on a copper grid. After the sample was scanned, appropriate areas were selected for the measurement of detailed two-dimensional (2-D) STEM−EELS images. An integrated energy range of 15 eV was used to quantify the EELS spectra.

2.3.5. X-ray Absorption Spectroscopy (XAS). XAS experiments were performed at beamline ID-26 of the European Synchrotron Radiation Facility (ESRF) in Grenoble, France. The energy of the incoming synchrotron radiation beam was selected with a Si(111) monochromator. The energy bandwidth of the incident X-ray beam was approximately 1.0 at 6500 eV, and the (maximum) incident total flux was 10^{13} photons/s. The incident energy was calibrated using tabulated values for the K edge features of a MnO standard. One flat and two focusing mirrors operating in total reflection were used to reject the higher harmonics. The Mn Kα fluorescence emission from the sample was collected using the (333) reflection of one spherically bent

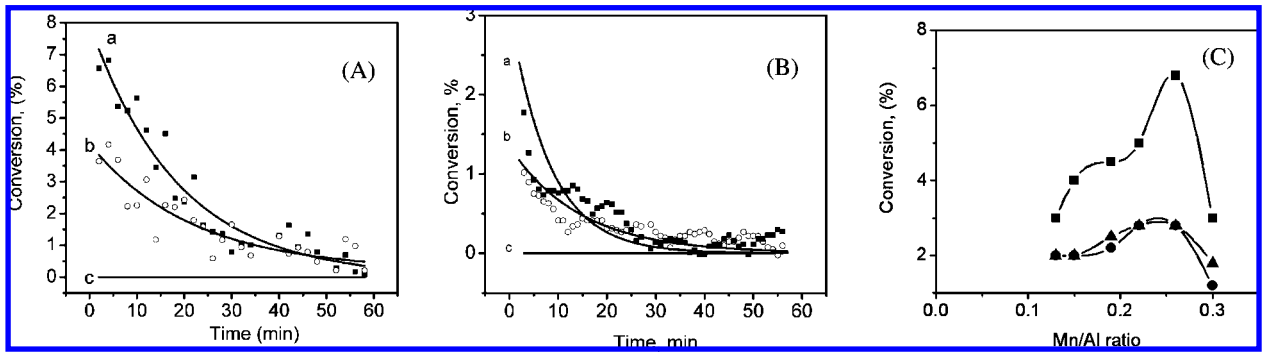

Figure 1. (A) N_2O and (B) NO conversion profiles for sample MnZ-0.26 (a, ■), MnZ-0.22 (b, ○), and MnZ-0.0 (c) during 1 h of N_2O exposure at 623 K, 3750 ppm N_2O, and 24 000 GHSV (h^{-1}). (C) Conversion of N_2O as a function of Mn/Al molar ratio for the first (■), second (▲), and third (●) catalytic cycle.

Ge crystal analyzer combined with an APD detector. The samples were pressed into self-supported wafers and placed in an airtight fluorescent cell at a position of 30° with respect to the incoming beam. XAS spectra measured with Mn Kα fluorescence are called high-energy-resolution fluorescence detection (HERFD) XAS, or HERFD-XAS, spectra, to distinguish them from normal XAS spectra.[43] HERFD-XAS removes the lifetime broadening of the 1s core state and effectively replaces it with the lifetime broadening of the 2p core state. This improves the Lorentzian broadening from ∼1.5 to ∼0.4 eV. The improved resolution allows a much improved separation of the pre-edge and edge region, allowing for much more detailed pre-edge analysis.[44–46] The in situ cell has a continuous gas flow during the measurements, allowing in situ XAS experiments. The edge jump of the Kα XAS spectra was normalized to one. Software PeakFit4 (AISN Software, 1995) was used to model the pre-edge region of the spectra. The pre-edge region was fitted using three pseudo-Voigt functions for all the spectra and also for the reference spectra. The first two functions were used to fit the pre-edge shapes of the spectrum, whereas the third pseudo-Voigt function was necessary for the fitting of the edge jump in combination with a Gaussian cumulative ascending function. The fit of the spectral shape was always with a R^2 value higher than 0.999. The extracted pre-edge data were used to determine the centroid energy position and integrated intensity. The extracted pre-edge data were used to determine the characteristics of the pre-edge, which is the centroid energy position and integrated intensity using the peak fitting results of the pre-edge feature. The centroid energy position is defined as the center of the gravity of the components and is calculated from the average position of the pseudo-Voigt functions weighted by their respective integrated areas.

2.4. Theory. The pre-edge spectral shapes of the Mn^{II} and Mn^{III} were calculated with charge transfer multiplet (CTM) calculations.[47] In octahedral symmetry, the pre-edge shape is given by the 1s3d transitions, where an Mn^{II} $3d^5$ ground state is excited to a $1s^13d^6$ final state. The shape for the tetrahedral symmetry is given by the contributions of the quadrupole and dipole transitions, where the intensity of the quadrupole transitions is assumed to be half of the intensity of the dipole transitions. This implies that the intensity of a tetrahedral symmetry peak is three times the intensity of an octahedral peak. The quadrupole final state is $1s^13d^6$, and the dipole final state $1s^13d^54p^1$. These states are not allowed to mix, unless the inversion symmetry is broken.[48] The crystal field splitting for Mn^{II} in octahedral or tetrahedral symmetry is assumed to be, respectively, +1.2 and −0.9 eV. For Mn^{III} in octahedral and tetrahedral symmetry, a $10Dq$ value of, respectively, +1.8 and −1.2 eV has been used. Due to the relative broad spectra, small variations in these values will not significantly modify the spectral shapes.

3. Results and Discussion

3.1. Catalytic Testing. Figure 1A shows the conversion of N_2O during the 1 h reaction time. The conversion decreases over the first hour. After ∼1 h the conversion goes to zero, implying that the active centers of the catalyst are consumed. The experiments using the undoped MnZ-0.00 sample show no reaction products, and the experiments on the N_2O decomposition indicate that thermal decomposition of N_2O occurs only above 698 K. We therefore conclude that no reaction occurs due to the ZSM-5 itself and that there is no thermal decomposition of N_2O, implying that the active phase of the catalyst is the manganese present in the ZSM-5 zeolite. The NO test reaction was performed after the N_2O decomposition at the same conditions of temperature and using a NO concentration of 3750 ppm. Figure 1B shows that the conversion has the same profile as the N_2O decomposition reaction. Blank experiment revealed that no reaction takes place when the undoped MnZ-0.00 sample was used. In addition, an experiment in which the N_2O decomposition step was omitted showed no reactivity of the sample toward NO oxidation reaction. This proves that, if NO oxidation takes place, it will be due to the action of the oxygen evolved in the N_2O decomposition step. The only product observed at the output of the reactor is NO_2. Similar to the N_2O reaction, the conversion of NO was followed during the reaction time.

Figure 1C shows the maximum conversion in the first three reaction cycles as a function of manganese loading. It can be seen that during the first run the initial conversions are significantly higher than in the second and third run. The second and third runs are equivalent, indicating a stable N_2O-NO conversion cycle. Note that the initial conversion for the MnZ-0.26 sample is significantly higher than for the other samples. The results for the second and third run follow a gradual increase up to the MnZ-0.26, where MnZ-0.30 has a much lower conversion.

During the N_2O decomposition, only N_2 is detected from the reactor outlet and no O_2 or other oxygen signal is detected. This effect can be explained with the help of the reaction mechanism. It is assumed that the mechanism reaction of N_2O decomposition occurs following the reactions:

$$N_2O_{(g)} + \bullet \leftrightarrow N_2O_{(ads)} \quad (1)$$

$$N_2O_{(ads)} \leftrightarrow N_{2(g)} + O_{(ads)} \quad (2)$$

$$2O_{(ads)} \leftrightarrows O_{2(g)} + 2\bullet \quad (3)$$

According to this reaction mechanism, both N_2 and O_2 should be detected during N_2O decomposition. The absence of O_2 demonstrates that step 3 does not take place, which implies that the evolving oxygen remains adsorbed to the catalyst. This effectively suggests that the N_2O decomposition reaction as such is stoichiometric. The created α-oxygen sites can be used by a hydrocarbon or NO, turning the combined system into a catalytic reaction. Knowing from blank experiments that the active phase is actually the manganese, we conclude that the O will remain adsorbed on the manganese center. The nature of the connection of this oxygen to the manganese is still to be determined. Taking into account that we know the amount of N_2O that is decomposed, we can quantify the amount of oxygen that is adsorbed on the manganese center. Calculations show that during the first cycle the atomic oxygen to manganese ratio (O/Mn) is 0.2 for MnZ-0.26. In the second and third cycles the O/Mn ratio is approximately 0.04 for all measured samples.

In order to see if the formed oxygen can be desorbed from the active center, the sample was heated to 773 K in a flow of inert gas. No oxygen was observed desorbing from the sample indicating that the oxygen is more strongly bound to Mn-ZSM-5 as compared to Fe-ZSM-5 and Cu-ZSM-5 materials. This is a behavior different from other α-oxygen-containing materials; the adsorbed oxygen can be desorbed at ~523 K for Fe-ZSM-5 materials[49] and at ~700 K for Cu-ZSM-5.[30]

3.2. Diffuse Reflectance Spectroscopy. Figure 2A shows the UV−vis DR spectra of MnZ-0.26 after a N_2O gas treatment (curve a) and after a subsequent treatment with NO (curve b), as described in the Experimental Section. Similar spectra have been obtained for all other samples. Analysis of the UV−vis DR spectrum of Mn-ZSM-5 suggests two transitions situated at ~16 000 and ~20 000 cm^{-1}, as is indicated in Figure 2B, where we used the MnZ-0.19 sample as example. It is evident from Figure 2A that after N_2O treatment a relatively intense absorption band appears at ~18 500 cm^{-1}. This band disappears when NO was flushed over Mn-ZSM-5, but it is restored with every N_2O treatment. The attempts to generate this band at temperatures below 623 K were unsuccessful. In addition, when instead of N_2O molecular oxygen was used in the temperature range of 298−673 K no UV−vis band has been observed.

We interpret this band as an indication of an elongated tetragonal Mn^{III} system, where these transitions relate to, respectively, $^5B_{1\,g} \rightarrow {}^5B_{2\,g}$ and $^5B_{1\,g} \rightarrow {}^5E_g$. For example, in $Mn(PO_3)_3$ these transitions occur at 18 870, respectively, 20 060 cm^{-1}, yielding a broad band situated at ~19 500 cm^{-1}.[24] In octahedral symmetry this relates to a $^5E_g \rightarrow {}^5T_{2\,g}$ transition, where the $T_{2\,g}$ states are split into $B_{2\,g}$ and E_g by the tetragonal distortion. The broad UV−vis structure as observed for the Mn-ZSM-5 systems could indicate that a range of distorted octahedral sites exist: A range of distortions would yield a series of sites that have transitions similar to $^5B_{1\,g} \rightarrow {}^5B_{2\,g}$ and $^5B_{1\,g} \rightarrow {}^5E_g$, but each with a slightly different energy. In addition, the shift of the band from ~19 500 cm^{-1} in $Mn(PO_3)_3$ to ~18 500 cm^{-1} in Mn-ZSM-5 systems could be related to the fact that metal ions in zeolites have smaller crystal field splittings than in bulk oxides.[50]

Figure 3 shows the integrated peak area (Figure 3A) and the average energy (Figure 3B) of the UV−vis DR band. It can be seen that the peak maximum is approximately constant between 18 000 and 18 500 cm^{-1} except for MnZ-0.10, where the absorption energy is ~17 000 cm^{-1}, which could indicate that

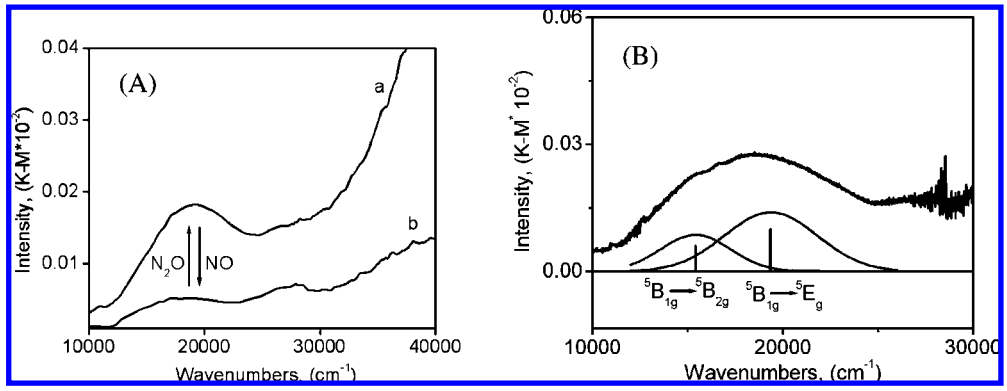

Figure 2. (A) UV−vis DR spectra of MnZ-0.26 after different gas treatments: curve a represents the sample after N_2O treatment at 623 K for 1 h, and curve b represents the sample after a subsequent NO treatment at 623 K for 1 h. (B) Fitted contributions of the 18 500 cm^{-1} of the MnZ-0.19 sample.

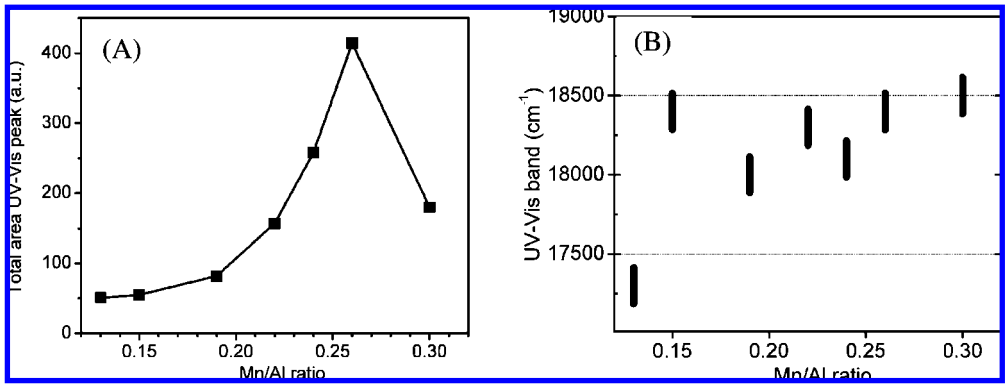

Figure 3. (A) The total area and (B) the average energy of the of the UV−vis DR band as a function of the Mn/Al molar ratio in Mn-ZSM-5 samples loaded with different amounts of Mn and treated in N_2O at 623 K for 1 h (solid squares).

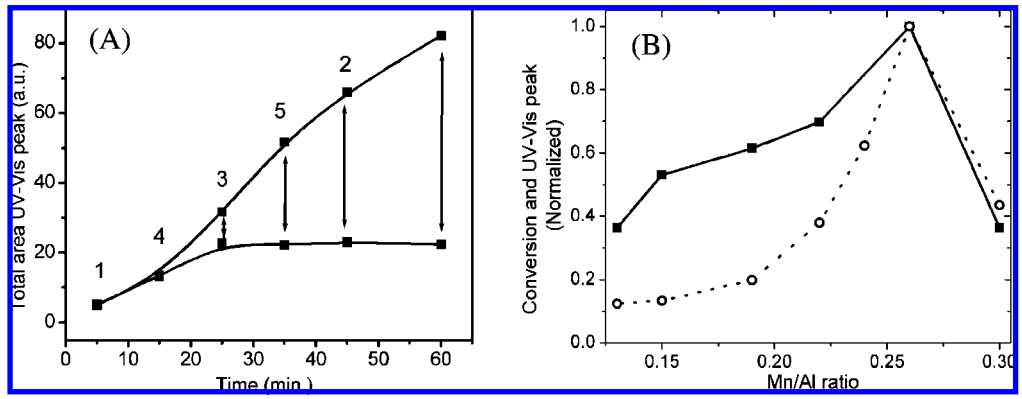

Figure 4. (A) Evolution of the total area for the 18 500 cm^{-1} UV−vis DR band for MnZ-0.19 during N_2O treatment measured at various time intervals and the consecutive NO treatment for the same period of time. The arrows indicate the decrease of the total area of the band during N_2O/NO treatment for the same time period. (B) The comparison of the integrated UV−vis DR band (dashed, ○) with the initial conversion in the first cycle (solid, ■), both normalized to 1.0.

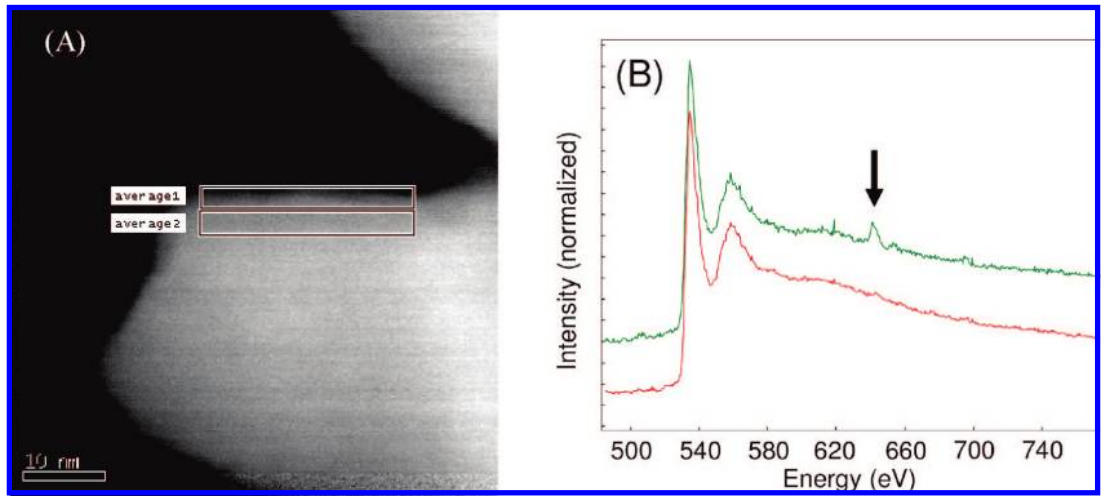

Figure 5. STEM image (A) indicating the surface (average 1) and bulk (average 2) regions. The Mn and Si L edge EELS spectra (B) of the surface (top line) and bulk (bottom line) of the zeolite. The arrow indicates the Mn L_3 edge.

for the lowest loadings the average sites have a smaller crystal field splitting. The total area of the 18 500 cm^{-1} peak increases with loading, reaching a maximum at a Mn/Al molar ratio of 0.26. Increasing the Mn/Al molar ratio further does result in a decrease of the 18 500 cm^{-1} UV−vis DR band intensity.

Figure 4A shows the experiment where we use shorter periods of the N_2O and the subsequent NO treatments. It can be observed that periods shorter than 1 h do not saturate the N_2O-induced effect and the band area. The NO treatment brings back the area to approximately one-quarter of the maximum value. An interesting finding is that the value after N_2O and NO treatments is the same for all time intervals, where the experiments at 5 and 15 min do not reach this value and show no effect from NO. This implies that in the first ∼20 min the sites are modified that are irreversible. Only after these sites have been used, the reversible sites are modified.

Figure 4B shows the comparison of the catalytic data from Figure 1C with the UV−vis DR band. There is a clear correspondence between both curves, indicating that there is a close link between the 18 500 cm^{-1} UV−vis DR band and the catalytic activity. The samples with loadings between 0.13 and 0.22 all have a significant conversion and, relatively, a small 18 500 cm^{-1} UV−vis DR band. Figure 4A indicates that approximately one-quarter of the 18 500 cm^{-1} UV−vis DR band remains while the catalytic activity has dropped to zero. This implies that part of the 18 500 cm^{-1} UV−vis DR band corresponds, not to active α-oxygen sites, but to nonactive sites that have a similar nature, i.e., Mn^{III} sites in a distorted octahedron.

3.3. STEM−EELS Measurements. We have measured the MnZ-0.24 sample with STEM−EELS. With the STEM dark field image the zeolite crystals have been mapped as indicated in Figure 5A. It turned out that this sample was rapidly destroyed by the electron beam, which made it impossible to measure reliable STEM−EELS line spectra and 2-D maps. Instead we have used the option to rapidly sweep over an area of the sample. Figure 5B shows two areas that were measured, where the average signal over the complete area is indicated as average 1 and average 2. Average 1 is positioned exactly at the surface and measures the spectrum of the top 2 nm of the ZSM-5 crystal (from −1 to +1 nm). The average 2 spectrum measures an area between 3 and 5 nm deep inside the sample. It can be seen in Figure 5B that the surface spectrum shows the presence of Mn, as indicated by the arrow. This peak relates to the Mn 2p EELS spectrum.[51] The spectrum taken at 3−5 nm inside the ZSM-5 shows no presence of manganese. We have measured a total of five different surfaces, where similar results have been found for three surfaces. Two other surfaces did not show a visible Mn signal for both its surface and subsurface spectrum, indicating that not all the ZSM-5 surfaces contain Mn in a detectable amount. These measurements suggest an enrichment of Mn at the surface of the zeolite crystals.

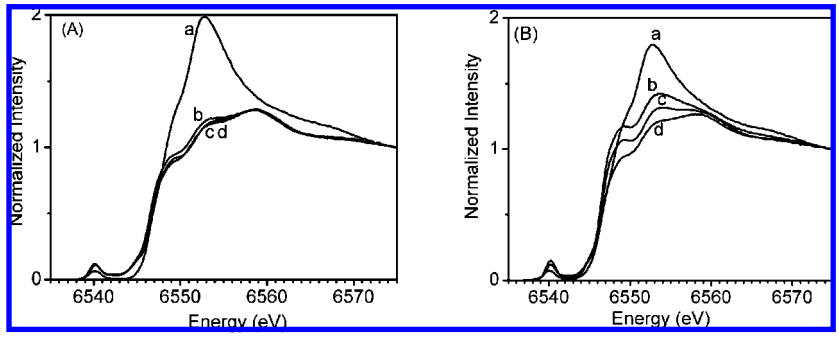

Figure 6. HERFD-XAS spectra at room temperature (a), 623 K (b), and after 1 h of N_2O (c) and NO treatment (d) of MnZ-0.24 (A) and MnZ-0.30 (B).

The STEM−EELS results indicate an enrichment of Mn at the zeolite surfaces. If we assume an average zeolite crystal as a prism with dimensions of 30 × 30 × 60 nm^3, the top 2 nm presents approximately 25% of the total volume, and assuming a uniform distribution of Al, one finds 25% of the Al ions in the top 2 nm. The samples have Mn/Al ratios between 0.13 and 0.30, which implies that it is possible that all Mn ions are attached to the Al ions in the top 2 nm of the sample, assuming that all Al sites are accessible. In this respect, we note that also the Al distribution over the zeolite crystal does not have to be uniform. In some experimental studies, Al also has a higher concentration at the surface of the crystal.[52] It seems that during the ion exchange the manganese will interact with the first Al-induced acid site that is available, forming a region with high concentration of manganese, which acts as a barrier and stops the migration into the zeolite channels. This can explain the fact that we could not obtain higher manganese loadings, even if we use higher concentration of manganese in solution.

3.4. HERFD-XAS Experiments. The Mn K edge XAS spectra of the samples have been measured. We show the results for MnZ-0.24 and MnZ-0.30. These samples have been measured at room temperature under He, after heating to 623 K (under He), and after each of the three N_2O and NO treatments. Figure 6 shows the XAS spectra, measured with the Kα HERFD technique. Heating to 623 K (a → b) decreases the white line. In addition, the edge shifts slightly and the pre-edge becomes smaller. The first N_2O treatment gives an edge shift of 1.83 eV, hence a slight oxidation, whereas the first NO treatment shows an inverse behavior and a slight reduction. A full analysis of these regions will be presented below. We will further analyze the various portions of these HERFD-XAS spectra below, respectively, the pre-edge region, the edge region, and the EXAFS region.

In a detailed and extensive XAS study on Mn-bearing minerals, Farges[53] presented a correlation of the changes of the Mn K pre-edge with the oxidation state and local symmetry. The pre-edge features of Mn in some 30 oxide materials were studied using this method. In order to make a quantitative determination of changes in the coordination of Mn based on variation of the pre-edge features high-resolution spectra are required for a well-resolved pre-edge structure and also a precise isolation of the pre-edge from the main edge. With the use of conventional XAS measurements inaccuracy is introduced due to the poor separation of the pre-edge region from the main edge, making a reliable and systematic background subtraction difficult. With the superior spectral resolution of HERFD-XAS a clear separation of these two regions is found, minimizing the inaccuracy. As an example, a comparison of the results (centroid position) obtained from the pre-edge analysis of two reference spectra (MnO and Mn_2O_3) measured using conventional, resonant inelastic X-ray scattering (RIXS) and HERFD-XAS techniques is shown in Table 1.

TABLE 1: Comparison between the Centroid Positions of Two Reference Compounds Calculated Based on Different Measuring XAS Techniques

method	ref	MnO	Mn_2O_3	ΔE
XAS	Farges[a]	6540.62	6540.91	0.3
HERFD-XAS	this work	6539.9	6541.6	1.7[b]

[a] Ref 53. [b] This value has been determined as 2.0 eV by Glatzel et al. (ref 54).

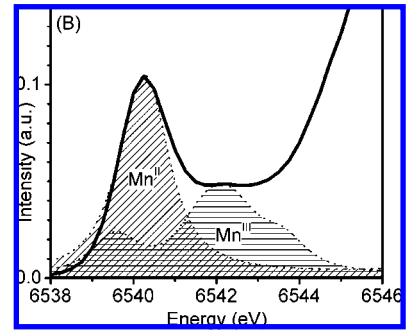

Figure 7. CTM calculations for 1s to 3d quadrupole transitions of Mn^{II} (diagonal lines) and Mn^{III} (horizontal lines) compared with the experimental pre-edge spectrum of MnZ-0.24-b.

The pre-edge feature of Mn^{II} has a distinct shape corresponding to the real spectrum and is situated at a low energy, which can be separated from the main edge. As we will show below, the Mn^{III} pre-edge feature consists of two strong features split by ∼3 eV, due to the large 3d3d multiplet interactions within the $1s^13d^5$ final state. The second feature is situated at a higher energy, and with normal XAS this feature will not be visible and will be included in the main edge. This explains the small shift between the two consecutive oxidation states compared with normal XAS to the high-resolution techniques.

The pre-edge spectrum of the Mn^{II} spectrum can be calculated from the transition from $3d^5$ to $1s^13d^6$, and the Mn^{III} spectrum is calculated from $3d^4 \rightarrow 1s^13d^5$. Figure 7 shows the results obtained from multiplet calculations, which corresponds well to reference compounds.[55] The calculated stick spectra are convoluted with a 1.1 eV Lorentzian and 1.2 eV Gaussian line shape to simulate, respectively, the lifetime broadening and the overall experimental resolution.[54] The broadened Mn^{II} pre-edge has a single peak related to two sticks split by the crystal field of 1.2 eV. The Mn^{III} $1s3d^5$ spectrum shows two features that are split by 3.0 eV. The first feature is close to the Mn^{II} peak, and the second feature appears at 6542 eV. Figure 7 shows the Mn^{II} and Mn^{III} calculated spectrum in comparison with the experimental pre-edge spectrum of MnZ-0.24-b. The Mn^{II} is

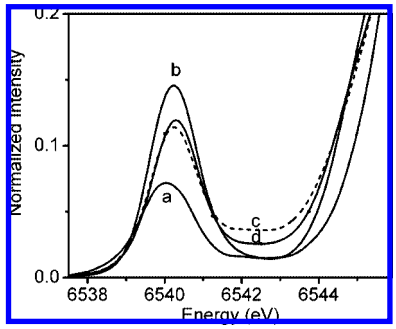

Figure 8. HERFD-XAS of MnZ-0.30 spectra at room temperature (a), 623 K (b), and after 1 h of N_2O (c, dotted) and NO treatment (d, solid with circles).

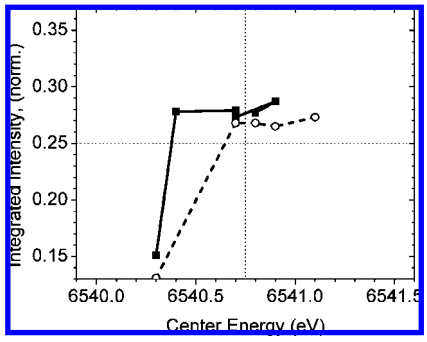

Figure 9. Integrated intensities and the center of gravity of the pre-edge of MnZ-0.30 (dashed, open circles) and MnZ-0.24 (solid, closed squares). The energy axis runs from the value of MnO (6539.9 eV) to the value of Mn_2O_3 (6541.6 eV). The integrated intensity spans the region between 0.13 for 6-fold coordination (octahedral) to 0.37 for 4-fold coordination (tetrahedral) symmetry. The dashed line indicates a 5-fold surrounding, respectively, a valence of 2.5.

clearly visible as the pre-edge peak, and presence of Mn^{III} can be related to the shoulder at 6542 eV.

Figure 8 shows an enlargement of the pre-edge regions of the XAS spectra. At room temperature, the sample is characterized by the presence of divalent manganese in a 6-fold coordination symmetry (spectrum a). At 623 K, the increase of the intensity in the pre-edge region shows that manganese is changing its symmetry, going from a 6-fold coordination to a 4-fold coordination[56,57] (spectrum b). This change from 6-fold to 4-fold symmetry is due to the elimination of the coordinated water. The first N_2O treatment increases the pre-edge to an average value between 4-fold and 6-fold. The subsequent NO and N_2O treatments keep the main pre-edge feature approximately constant, whereas the second feature at 6543 eV has an oscillating behavior function of the gas treatments (spectra c and d). To identify the nature of the features present in the pre-edge region multiplet calculations were performed for different oxidation states of manganese, i.e., a divalent and trivalent oxidation state.

Figure 9 presents the centroid positions and total integrated area obtained from the pre-edge analysis of the MnZ-0.30 and MnZ-0.24 samples through two N_2O−NO cycles. The center of gravity of Mn^{II} has been set to the value of MnO (6539.9 eV) and Mn^{III} to the value of Mn_2O_3 (6541.6 eV). The integrated intensity has been set to 0.13 for 6-fold (octahedral) and 0.37 for 4-fold (tetrahedral) symmetry, where these values have some variation from system to system.[56] Figure 9 shows that the samples start essentially as 6-fold Mn^{II} at room temperature. They change to 5-fold $Mn^{2.5+}$ at 623 K, where MnZ-0.30 is also partly oxidized. MnZ-0.30 oxidizes further under subsequent N_2O and NO treatments. In contrast, MnZ-0.24 is not oxidized during water loss. Its first N_2O treatment yields significant oxidation, and the subsequent steps have minor oxidizing (N_2O) and reducing (NO) effects.

This result indicates that the majority of the Mn sites are positioned in a 5-fold coordination with a valence of 2.5. After dehydration and the first N_2O oxidation, the effects of the N_2O and NO treatments on the MnZ-0.24 are minor. This indicates that the large majority of Mn sites remain in an average valence of 2.5 and a 5-fold coordination.

4. Conclusions

We have shown that we are able to prepare Mn-ZSM-5 zeolites that are active in the N_2O catalytic decomposition using an ion-exchange procedure. The material possessing maximum catalytic activity is characterized by a Mn/Al ratio of 0.26. The catalytic activity decreases to zero in 1 h and is significantly reduced in the second cycle. The initial activity relates to ∼30% α-oxygen sites per Mn atom, and the subsequent treatment with N_2O form approximately 4% α-oxygen sites, which are reversibly destroyed by the NO treatments.

An interesting result is that we find that the catalytic activity correlates with the intensity of a UV−vis band located at 18 500 cm^{-1}. Analysis suggests that this band correlates with Mn^{III} sites in a distorted tetragonal surrounding with a weaker crystal field, implying extended Mn−O bonds, than in bulk oxides. This 18 500 cm^{-1} band can be used as a marker for catalytic activity and as such for the presence of α-oxygen species. Initially N_2O creates stable oxidized sites in an amount of ∼4% of all the manganese atoms. Subsequently, the reversible α-oxygen sites are generated. The reactivity of this α-oxygen species was demonstrated using NO oxidation as a test reaction. The 18 500 cm^{-1} UV−vis band largely disappears after NO treatment, where the remaining intensity scales relates to the ∼4% inactive sites.

The STEM−EELS results indicate that the Mn sites are distributed unevenly over the ZSM-5 crystals. Most Mn atoms are found in the top ∼2 nm from the crystal surface, suggesting partial pore blocking for the exchange of Mn deeper inside the crystals.

The pre-edge analysis with HERFD-XAS indicates that heating to 623 K changes the coordination from 6-fold to 5-fold. The first N_2O causes reduction to a valence of approximately 2.5. The subsequent treatments with NO and N_2O cause only a minor change in the average Mn valence and coordination. This suggests a stable and static situation with the Mn atoms in a 5-fold coordination with a valence of 2.5. Approximately 4% of these Mn atoms are active and create α-oxygen sites during N_2O decomposition.

Acknowledgment. Financial support was provided by The Netherlands Organization for Scientific Research−Chemical Science (NWO−CW) and The Netherlands Research School Combination on Catalysis (NRSC-C). We acknowledge the European Synchrotron Radiation Facility for provision of synchrotron radiation facilities. The germanium crystal for the HERFD measurements was kindly provided by Professor Stephen P. Cramer.

References and Notes

(1) Panov, G. I.; Kharitonov, A. S.; Sobolev, V. I. *Appl. Catal., A* **1993**, *98*, 1.

(2) Centi, G.; Perathoner, S.; Arrigo, R.; Giordano, G.; Katovic, A.; Pedula, V. *Appl. Catal., A* **2006**, *307*, 30.

(3) Centi, G.; Perathoner, S.; Pino, F.; Arrigo, R.; Giordano, G.; Katovic, A.; Pedula, V. *Catal. Today* **2005**, *110*, 211.

(4) Hensen, E.; Zhu, Q. J.; Liu, P. H.; Chao, K. J.; van Santen, R. *J. Catal.* **2004**, *226*, 466.
(5) Kharitonov, A. S.; Aleksandrova, T. N.; Panov, G. I.; Sobolev, V. I.; Sheveleva, G. A.; Paukshtis, E. A. *Kinet. Catal.* **1994**, *35*, 270.
(6) Meloni, D.; Monaci, R.; Solinas, V.; Berlier, G.; Bordiga, S.; Rossetti, I.; Oliva, C.; Forni, L. *J. Catal.* **2003**, *214*, 169.
(7) Perathoner, S.; Pino, F.; Centi, G.; Giordano, G.; Katovic, A.; Nagy, J. B. *Top. Catal.* **2003**, *23*, 125.
(8) Selli, E.; Rossetti, I.; Meloni, D.; Sini, F.; Forni, L. *Appl. Catal., A* **2004**, *262*, 131.
(9) Sobolev, V. I.; Dubkov, K. A.; Paukshtis, E. A.; Pirutko, L. V.; Rodkin, M. A.; Kharitonov, A. S.; Panov, G. I. *Appl. Catal., A* **1996**, *141*, 185.
(10) Zhang, W. X.; Jia, M. J.; Zhang, C. L.; Zhang, L. H.; Wu, T. H.; Sun, T.; Yahiro, H.; Iwamoto, M. *Chem. J. Chin. Univ.* **1998**, *19*, 1112.
(11) Heijboer, W. M. Ph.D. Thesis, Utrecht University, 2005.
(12) Heijboer, W. M.; Koningsberger, D. C.; Weckhuysen, B. M.; de Groot, F. M. F. *Catal. Today* **2005**, *100*, 228.
(13) Dubkov, K. A.; Sobolev, V. I.; Panov, G. I. *Kinet. Catal.* **1998**, *39*, 72.
(14) Costine, A.; O'Sullivan, T.; Hodnett, B. K. *Catal. Today* **2005**, *99*, 199.
(15) (a) Weckhuysen, B. M.; Wang, D. J.; Rosynek, M. P.; Lunsford, J. H. *J. Catal.* **1998**, *175*, 338. (b) Weckhuysen, B. M.; Wang, D. J.; Rosynek, M. P.; Lunsford, J. H. *J. Catal.* **1998**, *175*, 347. (c) Weckhuysen, B. M.; Wang, D. J.; Rosynek, M. P.; Lunsford, J. H. *Angew. Chem., Int. Ed.* **1997**, *36*, 2374.
(16) Lebail, A.; Duroy, H.; Fourquet, J. L. *Mater. Res. Bull.* **1988**, *23*, 447.
(17) Melian-Cabrera, I.; Espinosa, S.; Groen, J. C.; van de Linden, B.; Kapteijn, F.; Moulijn, J. A. *J. Catal.* **2006**, *238*, 250.
(18) (a) Berlier, G.; Spoto, G.; Bordiga, S.; Ricchiardi, G.; Fisicaro, P.; Zecchina, A.; Rossetti, I.; Selli, E.; Forni, L.; Giamello, E.; Lamberti, C. *J. Catal.* **2002**, *208*, 64. (b) Berlier, G.; Prestipino, C.; Rivallan, M.; Bordiga, S.; Lamberti, C.; Zecchina, A. *J. Phys. Chem. B* **2005**, *109*, 22377.
(19) Tian, Y.; Ogawa, E.; Ikuo, A.; Shishido, T.; Zhang, Q. H.; Wang, Y.; Takehira, K.; Hasegawa, S. *Chem. Lett.* **2006**, *35*, 544.
(20) Zhu, Q.; Mojet, B. L.; Janssen, R. A. J.; Hensen, E. J. M.; van Grondelle, J.; Magusin, P.; van Santen, R. A. *Catal. Lett.* **2002**, *81*, 205.
(21) Battiston, A. A.; Bitter, J. H.; de Groot, F. M. F.; Overweg, A. R.; Stephan, O.; van Bokhoven, J. A.; Kooyman, P. J.; van der Spek, C.; Vanko, G.; Koningsberger, D. C. *J. Catal.* **2003**, *213*, 251.
(22) Heijboer, W. M.; Battiston, A. A.; Knop-Gericke, A.; Havecker, M.; Bluhm, H.; Weckhuysen, B. M.; Koningsberger, D. C.; de Groot, F. M. F. *Phys. Chem. Chem. Phys.* **2003**, *5*, 4484.
(23) Krishna, K.; Seijger, G. B. F.; van den Bleek, C. M.; Makkee, M.; Mul, G.; Calis, H. P. A. *Catal. Lett.* **2003**, *86*, 121.
(24) Pophal, C.; Yogo, T.; Tanabe, K.; Segawa, K. *Catal. Lett.* **1997**, *44*, 271.
(25) Pophal, C.; Yogo, T.; Yamada, K.; Segawa, K. *Appl. Catal., B* **1998**, *16*, 177.
(26) Chajar, Z.; Primet, M.; Praliaud, H. *J. Catal.* **1998**, *180*, 279.
(27) Gabelica, Z.; Valange, S. *Microporous Mesoporous Mater.* **1999**, *30*, 57.
(28) Groothaert, M. H.; Smeets, P. J.; Sels, B. F.; Jacobs, P. A.; Schoonheydt, R. A. *J. Am. Chem. Soc.* **2005**, *127*, 1394.
(29) Groothaert, M. H.; Battiston, A.; Wechuysen, B. M.; Schoonheydt, R. A. *J. Am. Chem. Soc.* **2003**, *125*, 7629.
(30) Groothaert, M. H.; Lievens, K.; van Bokhoven, J. A.; Battiston, A. A.; Weckhuysen, B. M.; Pierloot, K.; Schoonheydt, R. A. *ChemPhysChem* **2003**, *4*, 626.
(31) Groothaert, M. H.; Pierloot, K.; Delabie, A.; Schoonheydt, R. A. *J. Catal.* **2003**, *220*, 500.
(32) Yamashita, T.; Vannice, A. *J. Catal.* **1996**, *161*, 254.
(33) Singoredjo, L.; Korver, R.; Kapteijn, F.; Moulijn, J. *Appl. Catal., B* **1992**, *1*, 297.
(34) Kapteijn, F.; Rodriguez-Mirasol, J.; Moulijn, J. A. *Appl. Catal., B* **1996**, *9*, 25.
(35) Kapteijn, F.; Vanlangeveld, A. D.; Moulijn, J. A.; Andreini, A.; Vuurman, M. A.; Turek, A. M.; Jehng, J. M.; Wachs, I. E. *J. Catal. Lett.* **1994**, *150*, 94.
(36) Kapteijn, F.; Singoredjo, L.; Vandriel, M.; Andreini, A.; Moulijn, J. A.; Ramis, G.; Busca, G. *J. Catal.* **1994**, *150*, 105.
(37) Kapteijn, F.; Singoredjo, L.; Andreini, A.; Moulijn, J. A. *Appl. Catal., B* **1994**, *3*, 173.
(38) Singoredjo, L.; Kapteijn, F. *Stud. Surf. Sci. Catal.* **1993**, *75*, 2705.
(39) Kapteijn, F.; Singoredjo, L.; Dekker, N. J. J.; Moulijn, J. A. *Ind. Eng. Chem. Res.* **1993**, *32*, 445.
(40) Cimino, A.; Bosco, R.; Indovina, V.; Schiavello, M. *J. Catal.* **1966**, *5*, 271.
(41) Stone, F. S. *J. Solid State Chem.* **1975**, *12*, 271.
(42) Teunissen, W.; de Groot, F. M. F.; Geus, J.; Stephan, O.; Tence, M.; Colliex, C. *J. Catal.* **2001**, *204*, 169.
(43) Glatzel, P.; Bergmann, U. *Coord. Chem. Rev.* **2005**, *249*, 65.
(44) de Groot, F. *Chem. Rev.* **2001**, *101*, 1779.
(45) de Groot, F. M. F.; Glatzel, P.; Bergmann, U.; van Aken, P. A.; Barrea, R. A.; Klemme, S.; Hävecker, M.; Knop-Gericke, A.; Heijboer, W. M.; Weckhuysen, B. M. *J. Phys. Chem. B* **2005**, *109*, 20751.
(46) de Groot, F. M. F.; Krisch, M. H.; Vogel, J. *Phys. Rev. B* **2002**, 66.
(47) de Groot, F. M. F. *Chem. Rev.* **2001**, *101*, 1779.
(48) Westre, T. E.; Kennepohl, P.; DeWitt, J. G.; Hedman, B.; Hodgson, K. O.; Solomon, E. I. *J. Am. Chem. Soc.* **1997**, *119*, 6297.
(49) Panov, G. I.; Sobolev, V. I.; Kharitonov, A. S. *J. Mol. Catal.* **1990**, *61*, 85.
(50) Heijboer, W. M.; Battiston, A. A.; Knop-Gericke, A.; Havecker, M.; Mayer, R.; Bluhm, H.; Schlogl, R.; Weckhuysen, B. M.; Koningsberger, D. C.; de Groot, F. M. F. *J. Phys. Chem. B* **2003**, *107*, 13069.
(51) de Groot, F. M. F.; Fuggle, J. C.; Thole, B. T.; Sawatzky, G. A. *Phys. Rev. B* **1990**, *42*, 5459.
(52) Dessau, R. M.; Valyocsik, E. W.; Goeke, N. H. *Zeolites* **1992**, *12*, 776.
(53) Farges, F. *Phys. Rev. B* **2005**, *71*, 155109.
(54) Glatzel, P.; Bergmann, U.; Yano, J.; Visser, H.; Robblee, J. H.; Gu, W.; de Groot, F. M. F.; Christou, G.; Pecoraro, V. L.; Cramer, S. P.; Yavhandra, V. K. *J. Am. Chem. Soc.* **2004**, *126*, 9946.
(55) De Groot, F.; Kotani, A. *Core Level Spectroscopy of Solids*; Taylor and Francis: New York, 2008.
(56) Heijboer, W. M.; Glatzel, P.; Sawant, K. R.; Lobo, R. F.; Bergmann, U.; Barrea, R. A.; Koningsberger, D. C.; Weckhuysen, B. M.; de Groot, F. M. F. *J. Phys. Chem. B* **2004**, *108*, 10002.
(57) Wilke, M.; Farges, F.; Petit, P. E.; Brown, G. E.; Martin, F. *Am. Mineral.* **2001**, *86*, 714.

JP802915K